Geophysical Journal International

Geophys. J. Int. (2025) **243,** 1–15
Advance Access publication 2025 September 01
Research Paper

https://doi.org/10.1093/gji/ggaf339

Seafloor fibre optical cable repositioning using target motion analysis on distributed acoustic sensing of underwater acoustic noise

Diane Rivet [1], Lucas Papotto,[1,2] Benoit de Cacqueray[2] and Jean-Paul Ampuero [1]

[1]*Observatoire de la Côte d'Azur, Université Côte d'Azur, CNRS, IRD, Géoazur, 250 rue Albert Einstein, Sophia Antipolis 06560 Valbonne, France.. E-mail: diane.rivet@geoazur.unice.fr*
[2]*Thales Defense Mission System,* 525 *Route des Dolines,* F-06560 *Valbonne, France*

Accepted 2025 August 13. Received 2025 August 12; in original form 2025 March 26

SUMMARY

Distributed acoustic sensing (DAS) is a recent technology that turns optical fibres into multisensor arrays. In the marine environment, it offers new possibilities for measuring seismic and environmental signals. While DAS can be applied to existing fibre optic cables used for communications, a major limitation of such efforts is that the position of the cable is not always known with sufficient accuracy. In particular, for submarine telecommunication cables, the positioning accuracy decreases with increasing depth. This problem affects the accuracy of earthquake locations and source parameters based on DAS signals. This limitation calls for methods to retrieve the cable's position and orientation. Here, we propose a method for relocating a linear section of cable—or multiple connected segments—using incidental acoustic sources, particularly boats moving in the vicinity of the cable. The method is based on target motion analysis (TMA) for sources in uniform rectilinear motion. We consider Bearing-Only TMA (BO-TMA) and the Bearing and Frequency TMA (BF-TMA), which respectively use changes in backazimuth (called bearing in navigation) and changes in both backazimuth and Doppler frequency shift as the source moves. We adapt these methods to the 3-D case to account for the difference in depth between the fibre and the sources. Both cases lead to a nonlinear inverse problem, which we solve by the Levenberg–Marquardt method. On synthetic data, we test both TMA techniques on single and multiple source trajectories and evaluate their accuracy as a function of source trajectory and velocity. We then test the BO-TMA on real DAS recordings of acoustic signals produced by passing ships near a 42 km-long fibre optic cable off the coast of Toulon, southeastern France. In this study case, the position and characteristics of the acoustic source are known. While the Doppler frequency shift at low frequency (30 Hz) is difficult to measure with sufficient accuracy ($< 0.1^{\circ}$), we demonstrate that effective cable location can be achieved by BO-TMA using multiple ship passages with a variety of trajectories. Once the linear sections of the cable have been relocated, the stage is set to reconstruct the entire cable configuration. More generally, the 3-D TMA on linear antennas developed here can be used to locate either the sources or the antenna situated at different depths.

Key words: Inverse theory; Acoustic emission; Distributed acoustic sensing.

1 INTRODUCTION

Distributed acoustic sensing (DAS) transforms existing fibre optic cables into antennas sensitive to longitudinal (along-cable) strain or strain rate, on a broad frequency band and with metre-scale resolution over distances exceeding one hundred kilometres (Rao *et al.* 2021; Waagaard *et al.* 2021). A DAS interrogator connected to one end of the cable sends repeated laser pulses into the fibre, records the Rayleigh backscattered light from the fibre's inherent impurities (Hartog 2017), and applies optical and digital processing to measure the effect of environmental disturbances on the cable's optical fibre. The ability to connect the interrogator at an onshore cable termination of the cable makes DAS much easier and more economical to deploy and maintain than traditional marine instrumentation such as ocean-bottom seismometers (OBS), hydrophones or pressure sensors, which typically require costly vessel-based deployment and periodic recovery for maintenance or data retrieval. Moreover, if real-time data acquisition is needed, these conventional instruments

must be connected to shore via dedicated seafloor cables for power supply and data transmission, significantly increasing installation complexity and cost.

Originally developed in the oil and gas industry (Mateeva *et al.* 2014a; Parker *et al.* 2014; Ashry *et al.* 2022), distributed acoustic sensing (DAS) has been widely utilized for approximately a decade in crustal-scale seismology on land. This technology employs dedicated cables or telecom dark fibre (Daley *et al.* 2013; Dou *et al.* 2017; Jousset *et al.* 2018) as well as operational telecom cables (Brenne *et al.* 2024). The expansion of DAS applications to underwater environments, leveraging submarine telecom cables, has yielded extensive observations about the solid Earth and its interactions with the ocean (Lindsey *et al.* 2019; Sladen *et al.* 2019; Williams *et al.* 2019). These observations encompass a range of phenomena, including small-scale local seismicity, teleseismic earthquakes, ocean gravity waves and microseismic noise (e.g. Lior *et al.* 2021; Fernández-Ruiz *et al.* 2022; Guerin *et al.* 2022; Mazur *et al.* 2024), achieving unprecedented spatial resolution. Furthermore, DAS data collected on the ocean floor has enhanced our understanding of the underwater environment. This includes monitoring deep-sea currents (Mata Flores *et al.* 2023), detecting internal waves and seabed temperatures (Matsumoto *et al.* 2021; Pelaez Quiñones *et al.* 2023), tracking marine mammals (Bouffaut *et al.* 2022; Landrø *et al.* 2022), and observing anthropogenic noise such as maritime traffic (Rivet *et al.* 2021), as well as meteorological phenomena like storms (Taweesintananon *et al.* 2023).

The potential to utilize thousands of kilometres of pre-existing telecommunication cables makes DAS a cost-effective technology. However, one of the limiting factors in the use of existing cables is the inaccurate knowledge of their location. Telecommunication companies may lack precise route information or may be reluctant to share it due to the sensitive nature of their infrastructure. For decommissioned cables, it is sometimes impossible to find any documentation of the cable deployment. For recent cables, it may be possible to obtain the route taken by the cable-laying vessel during deployment, but the map-view position of the cable can change between its release and its final resting position on the seabed. Large layback, current drift, seafloor bathymetry and slack in the cable, can result in uncertainties on the touchdown cable position that can range from 2 per cent to 20 per cent of the water depth (Andres 1998; Mamatsopoulos *et al.* 2020). As we will later show in our own case study, we observe a comparable magnitude of uncertainty—approximately 400 m.

An accurate knowledge of the submarine cable position is essential to minimize uncertainties in the analysis of DAS data. In the study by Trabattoni *et al.* (2024), which focuses on a submarine cable in Chile, residual traveltime differences were identified that could plausibly be attributed, at least in part, to cable mislocation and lateral velocity variations in deeper structures. These residuals—after correcting for lateral variations in the sedimentary cover—can reach up to 0.1 s for P waves and 0.3 s for S waves. Although lateral variations in deeper velocity structure cannot be ruled out, the observed residuals are consistent with local cable position uncertainties on the order of a few hundred metres.

Minimizing positioning errors to less than 100 m would enhance the full potential of distributed acoustic sensing (DAS) technology. This improvement would not only enable more accurate imaging of deeper velocity structures through traveltime tomography (e.g. Biondi *et al.* 2023b) but also improve the precision of the event locations. Previous studies have addressed cable relocation using DAS data in both underwater and terrestrial environments, employing GPS-tracked sources for accurate positioning. Shao *et al.* (2025) demonstrated ship tracking using frequency shifts extracted via synchrosqueezing transform on offshore DAS cables, while Biondi *et al.* (2023a) achieved precise geolocation of DAS channels on land cables by combining DAS with GPS-tracked vehicles. Here, we address this issue by using sources of acoustic signals with known location, such as boats, to reposition and reorient submarine cables.

Several sensor relocation methods have been developed and effectively applied for underwater acoustic sensor arrays and ocean bottom seismometers. One such method utilizes the direction of arrival of waves, estimated through array processing, whose ultimate precision (the so-called Cramer-Rao bound) depends on the array geometry (e.g. Gazzah & Marcos 2005; Gera & Mulgrew 2009). Cepstrum signal analysis, which exploits multiple wave paths in the water column, has also been applied effectively (Gao *et al.* 2008; Ferguson *et al.* 2019; Trabattoni *et al.* 2020). Cross-correlation techniques to retrieve the relative position between sensors in a hydrophone array demonstrated their effectiveness particularly on broad-band signals (Sabra *et al.* 2005). In the absence of controlled acoustic sources, the use of ship noise has proven useful to relocate the elements of a linear antenna at shallow depth (Gemba *et al.* 2018) and ocean bottom seismometers (Trabattoni *et al.* 2020).

In this study we develop a sensor relocation method for optical fibre cables in deep water using acoustic noise emitted by boats. Here, the cable is transformed into a sensor arrays by DAS. As shown by Rivet *et al.* (2021), boat noise is detectable even at great depths ($>$ 1 km) at frequencies below 50 Hz. This noise has a specific signature consisting of distinct frequencies and their respective harmonics. The boat analysed by the authors in their example had indeed several spectral lines at 16, 33, 41, 49, 57, 76 and 83 Hz. Because boats broadcast their location and velocity through their automatic identification system (AIS), they serve as effective acoustic sources. We extend and adapt 2-D passive trajectography principles, such as those developed by Nardone *et al.* (1984), Passerieux *et al.* (1988), Ho & Chan (2006a), Pillon & Jauffret (2005) and Chan & Rudnicki (1992), to perform the relocation of a fix cable using moving sources. The method we develop here is specifically designed for linear cable segments and determines both the location of the centre of the selected cable segment and its orientation.

We first introduce and adapt in Section 2 the basic principles of passive trajectography using angle and frequency measurements—Bearing and Frequency TMA (BF-TMA)—to the 3-D case, where both the source and the antenna may lie at different depths. A nonlinear solver is used to tackle the resulting inverse problem. We then extend the method to the relocation of multiple cable segments, introducing regularization to ensure spatial and angular continuity between the segments. At this stage, the method is demonstrated on simulated time-series in Section 3, where we evaluate its performance. In Section 4, we apply the approach to real DAS data recorded on a seafloor cable off the coast of Toulon, France, and relocate a linear section of the cable. In the same section, we also test the method on a synthetic case that mimics the real configuration, using multiple sources and multiple cable segments.

2 3-D BEARING AND FREQUENCY TARGET MOTION ANALYSIS FOR FIBRE OPTIC CABLE RELOCATION

2.1 Application to distributed acoustic sensing and cable relocation

We utilize target motion analysis (TMA) to relocate sections of a seafloor fibre optic cable based on acoustic time-series acquired

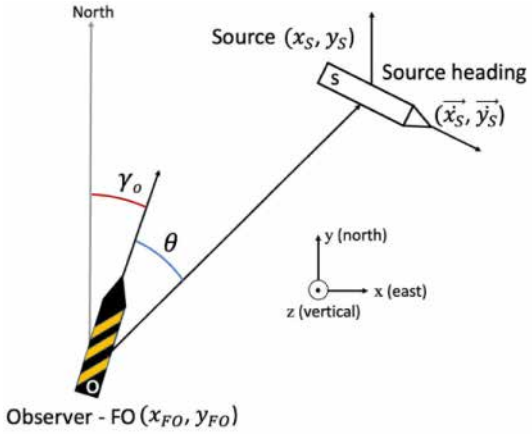

Figure 1. Map view of the reference frame for the bearing measurement of a moving source by a fixed observer.

using DAS during the passage of a boat in the vicinity of the cable. Hereafter, the boat is designated as the source and the selected segment of the fibre optic cable is designated as the observer.

We consider a 3-D reference frame, with the $\vec{x}$ axis pointing east, the $\vec{y}$ axis pointing north and the $\vec{z}$ axis pointing vertically upwards (Fig. 1). The observer is characterized by the position of its centre $(x_{\rm FO}, y_{\rm FO}, 0)$ and its orientation relative to the north, $\gamma_{\rm FO}$. We ignore the slope of the seafloor and assume that the cable is horizontal. We define the state vector $\mu_{\rm DAS} = (x_{\rm FO}, y_{\rm FO}, \gamma_{\rm FO})$, which contains the state parameters of the observer we aim to determine. The source position is determined using AIS data sampled at 5-min intervals. Between these 5-min intervals, we assume that the source moves with uniform rectilinear motion (URM). We further assume the water depth, h, is constant and known. At any given time $t_i = iT$, where T is the time-step, the source position is known and determined by its initial position (x_{s_0}, y_{s_0}, h) and constant velocity $\vec{v_s} = (\dot{x}_s, \dot{y}_s, 0)$ as

$$\begin{aligned} x_s(i) &= x_{s_0} + iT\dot{x}_s \\ y_s(i) &= y_{s_0} + iT\dot{y}_s. \end{aligned} \tag{1}$$

2.2 Pseudo-bearing and frequency measurements

To determine the observer's position and orientation, we measure the angle θ in 3-D the observer's orientation (the cable axis) and the cable-source direction, referred to as the pseudo-bearing, as well as the Doppler frequency shift, which is the change in frequency of the acoustic wave observed when there is relative motion between the source and the observer.

There are multiple possible source locations compatible with a given θ value; they lie along the intersection (a hyperbola) between the water surface and the angle cone θ around the cable axis (Fig. 2, red line).

Since DAS transforms a fiber optic cable into a linear sensor array, we perform beamforming on DAS data to estimate pseudo-bearing and frequency. Numerous beamforming methods have been developed over the decades (Cox *et al.* 1987; Van Veen & Buckley 1988) and more recently, they have been applied to DAS, notably in seismic studies (Nayak *et al.* 2021; van den Ende & Ampuero 2021; Guerin *et al.* 2022). Here, we choose to perform beamforming in the frequency domain (Boué *et al.* 2013) because it preserves the direction of propagation, including its sign, which is often lost in time-domain approaches. Additionally, frequency-domain beamforming enables us to identify the most coherent frequency component across the array and to measure the Doppler shift associated with the relative motion between the source and the observer.

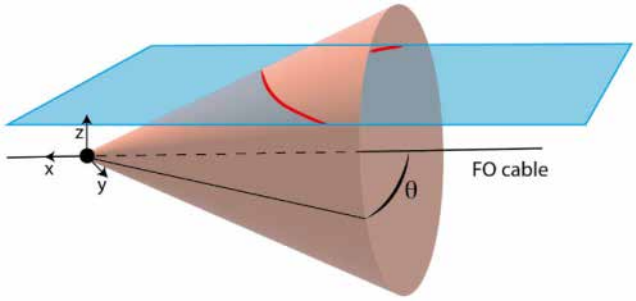

Figure 2. For a given pseudo-bearing angle θ, the admissible source locations are situated along the intersection between the water surface and the cone of revolution of angle θ around the cable axis, displayed by a red line.

2.3 Pseudo-bearing misfit in 3-D TMA

We express the pseudo-bearing as a function of the state parameters. The scalar product between the unit vector along the cable, $\vec{o} = (\sin\gamma_{\rm FO}, \cos\gamma_{\rm FO}, 0)$, and the position of the source relative to the centre of the cable section, $\vec{s} = (x_s - x_{\rm FO}, y_s - y_{\rm FO}, h)$, is:

$$\vec{o} \cdot \vec{s} = ||\vec{s}|| \cos\theta. \tag{2}$$

Thus,

$$\cos\theta = \frac{(y_s - y_{\rm FO})\cos\gamma_{\rm FO} + (x_s - x_{\rm FO})\sin\gamma_{\rm FO}}{\sqrt{(x_s - x_{\rm FO})^2 + (y_s - y_{\rm FO})^2 + h^2}}. \tag{3}$$

The pseudo-bearing θ_i measured at time t_i includes bearing measurement errors. We define the pseudo-bearing misfit ε_{θ_i} as the difference between the measured pseudo-bearing cosine $\cos\theta_i$ and the one predicted by eq. (3):

$$\varepsilon_{\theta_i} = \cos\theta_i - \frac{(y_{s_i} - y_{\rm FO})\cos\gamma_{\rm FO} + (x_{s_i} - x_{\rm FO})\sin\gamma_{\rm FO}}{\sqrt{(x_{s_i} - x_{\rm FO})^2 + (y_{s_i} - y_{\rm FO})^2 + h^2}}. \tag{4}$$

2.4 Frequency error in 3-D TMA

The apparent source frequency f measured by the observer, subjected to the Doppler effect, is

$$\frac{f}{f_s} = 1 + \frac{v_{\rm proj}}{c_0}, \tag{5}$$

where f_s is the real source frequency that can be determined from a spectrogram of the signal recorded by sensors assumed to be near the boat's passage, c_0 the acoustic wave speed and $v_{\rm proj}$ the projection of the source velocity onto the observer-to-source direction:

$$v_{\rm proj} = \vec{v_s} \cdot \vec{s}/||\vec{s}||. \tag{6}$$

Expanding, we get

$$v_{\rm proj} = \frac{(x_s - x_{\rm FO})\dot{x}_s + (y_s - y_{\rm FO})\dot{y}_s}{\sqrt{(x_s - x_{\rm FO})^2 + (y_s - y_{\rm FO})^2 + h^2}}. \tag{7}$$

Then, we can express the frequency shift as

$$\frac{f}{f_s} = 1 + \frac{(x_s - x_{\rm FO})\dot{x}_s + (y_s - y_{\rm FO})\dot{y}_s}{c_0\sqrt{(x_s - x_{\rm FO})^2 + (y_s - y_{\rm FO})^2 + h^2}}. \tag{8}$$

The apparent frequency f_i measured at time t_i includes frequency measurement errors. We define the frequency misfit ε_{f_i} as the difference between the normalized measured frequency f_i/f_s and the one predicted by eq. (8):

$$\varepsilon_{f_i} = \frac{f_i}{f_s} - 1 - \frac{(x_{s_i} - x_{\mathrm{FO}})\dot{x}_s + (y_{s_i} - y_{\mathrm{FO}})\dot{y}_s}{c_0\sqrt{(x_{s_i} - x_{\mathrm{FO}})^2 + (y_{s_i} - y_{\mathrm{FO}})^2 + h^2}}. \tag{9}$$

2.5 Nonlinear least-square inversion

We aim to find the values of the state parameters that minimize an objective function defined as the sum of the L_2 norms of the pseudo-bearing and Doppler shift error vectors, $\{\varepsilon_{\theta_i}\}_{i=1,\cdots,N_{\mathrm{obs}}}$ and $\{\varepsilon_{f_i}\}_{i=1,\cdots,N_{\mathrm{obs}}}$, respectively, where N_{obs} is the number of observations of the source.

We define the observed data vector $\mathbf{d} \in \mathbb{R}^{2N_{\mathrm{obs}}}$ as the concatenation of the pseudo-bearing angles θ_i and apparent frequencies f_i measured at times t_i, for $i = 1, \ldots, N_{\mathrm{obs}}$. Thus, the data vector is written as:

$$\mathbf{d} = \begin{bmatrix}\theta_1 & f_1 & \theta_2 & f_2 & \cdots & \theta_{N_{\mathrm{obs}}} & f_{N_{\mathrm{obs}}}\end{bmatrix}^\top \in \mathbb{R}^{2N_{\mathrm{obs}}}. \tag{10}$$

Note that when we consider only bearing BO-TMA, $\mathbf{d} \in \mathbb{R}^{N_{\mathrm{obs}}}$.

The model prediction $\mathbf{G}(\mathbf{m})$ is the matrix product of $\mathbf{m}$ is the state vector of N_{param} model parameters containing the central position $(x_{\mathrm{FO}}, y_{\mathrm{FO}})$ and azimuthal angle γ_{FO} to be determined

$$\mathbf{m} = \begin{bmatrix}x_{\mathrm{FO}} & y_{\mathrm{FO}} & \gamma_{\mathrm{FO}}\end{bmatrix} \in \mathbb{R}^{N_{\mathrm{param}}} \tag{11}$$

and $\mathbf{G}$ the nonlinear system of $2 \times N_{\mathrm{obs}}$ equations that define the forward problem (eqs 3 and 8). The objective function to be minimized is

$$S(\mathbf{m}) = ||\mathbf{G}(\mathbf{m}) - \mathbf{d}||^2 = \sum_{i=1}^{m}(G_i(\mathbf{m}) - d_i)^2. \tag{12}$$

The objective function depends nonlinearly on $\mathbf{m}$. To solve this nonlinear least-squares problem, we use the Levenberg–Marquardt (L-M) method. This approach is an improvement over the Gauss–Newton method that solves the nonlinear problem by approximating the exact Hessian matrix with its Jacobian matrix, avoiding the high cost of computing the second derivatives of the objective function (e.g. Pratt *et al.* 1998). The L-M method transitions between a gradient descent far from the solution and Gauss–Newton near the solution.

We iteratively update the model parameters, starting with an initial guess $\mathbf{m}^0$, as

$$\mathbf{m}^{k+1} = \mathbf{m}^k + \Delta\mathbf{m}^{k+1}, \tag{13}$$

where $\Delta\mathbf{m}^{k+1}$ satisfies the normal equations

$$\Delta\mathbf{m}^{k+1} = -(J^T J - \lambda I)^{-1} J^T(\mathbf{G}(\mathbf{m}^k) - \mathbf{d}), \tag{14}$$

where J is the Jacobian matrix of size $(2N_{\mathrm{obs}}, N_{\mathrm{param}})$:

$$J = \begin{pmatrix} \frac{\partial\varepsilon_{f_1}}{\partial x_{\mathrm{FO}}} & \frac{\partial\varepsilon_{f_1}}{\partial y_{\mathrm{FO}}} & \frac{\partial\varepsilon_{f_1}}{\partial\gamma_{\mathrm{FO}}} \\ \frac{\partial\varepsilon_{\theta_1}}{\partial x_{\mathrm{FO}}} & \frac{\partial\varepsilon_{\theta_1}}{\partial y_{\mathrm{FO}}} & \frac{\partial\varepsilon_{\theta_1}}{\partial\gamma_{\mathrm{FO}}} \\ \cdots & \cdots & \cdots \\ \cdots & \cdots & \cdots \\ \frac{\partial\varepsilon_{f_{N_{\mathrm{obs}}}}}{\partial x_{\mathrm{FO}}} & \frac{\partial\varepsilon_{f_{N_{\mathrm{obs}}}}}{\partial y_{\mathrm{FO}}} & \frac{\partial\varepsilon_{f_{N_{\mathrm{obs}}}}}{\partial\gamma_{\mathrm{FO}}} \\ \frac{\partial\varepsilon_{\theta_{N_{\mathrm{obs}}}}}{\partial x_{\mathrm{FO}}} & \frac{\partial\varepsilon_{\theta_{N_{\mathrm{obs}}}}}{\partial y_{\mathrm{FO}}} & \frac{\partial\varepsilon_{\theta_{N_{\mathrm{obs}}}}}{\partial\gamma_{\mathrm{FO}}} \end{pmatrix} \tag{15}$$

Setting

$$x = (x_{s_i} - x_{\mathrm{FO}}) \tag{16}$$

$$y = (y_{s_i} - y_{\mathrm{FO}}) \tag{17}$$

$$R = \sqrt{x^2 + y^2 + h^2} \tag{18}$$

we write the derivatives for pseudo-bearing misfits as

$$\frac{\partial\varepsilon_{\theta_i}}{\partial x_{\mathrm{FO}}} = \frac{\sin\gamma_{\mathrm{FO}}(y^2 + h^2) - xy\cos\gamma_{\mathrm{FO}}}{R^3} \tag{19}$$

$$\frac{\partial\varepsilon_{\theta_i}}{\partial y_{\mathrm{FO}}} = \frac{\cos\gamma_{\mathrm{FO}}(x^2 + h^2) - xy\sin\gamma_{\mathrm{FO}}}{R^3} \tag{20}$$

$$\frac{\partial\varepsilon_{\theta_i}}{\partial\gamma_{\mathrm{FO}}} = \frac{y\sin\gamma_{\mathrm{FO}} - x\cos\gamma_{\mathrm{FO}}}{R} \tag{21}$$

and for frequency misfits as

$$\frac{\partial\varepsilon_{f_i}}{\partial x_{\mathrm{FO}}} = \frac{\dot{x}_s}{c_0 R} - \frac{x(\dot{x}_s x + \dot{y}_s y)}{c_0 R^3} \tag{22}$$

$$\frac{\partial\varepsilon_{f_i}}{\partial y_{\mathrm{FO}}} = \frac{\dot{y}_s}{c_0 R} - \frac{y(\dot{x}_s x + \dot{y}_s y)}{c_0 R^3} \tag{23}$$

$$\frac{\partial\varepsilon_{f_i}}{\partial\gamma_{\mathrm{FO}}} = 0. \tag{24}$$

We incorporate data measurement errors through a weighted least-squares approach. We assume that the measurement errors follow a normal distribution with a standard deviation σ_i. The objective function is replaced by

$$S(\mathbf{m}) = \sum_{i=1}^{m}(G_i(m) - d_i)^2/\sigma_i^2. \tag{25}$$

Because pseudo-bearing misfits are expressed as cosine residuals, we compute their standard deviation using the error propagation method. The resulting weighted pseudo-bearing misfit is

$$\varepsilon_{\theta w_i} = \frac{\varepsilon_{\theta_i}}{\sin(\theta_i)\sigma_{\theta i}} \tag{26}$$

with $\sigma_{\theta i}$ in radian. Accordingly, the components of the Jacobian corresponding to the pseudo-bearing misfit are normalized by $\sin(\theta_i)\sigma_{\theta i}$. Similarly, the weighted frequency misfits are

$$\varepsilon_{f w_i} = \frac{f_s\varepsilon_{f_i}}{\sigma_{f i}} \tag{27}$$

and their Jacobian components are normalized by $\sigma_{f i}/f_s$.

The objective function $S(\mathbf{m})$ provides useful statistical information about the quality of the model estimates. Since $S(\mathbf{m})$ depends on normally distributed random errors in $\mathbf{d}$, it is a random variable and has a χ^2 distribution with $N_{\mathrm{obs}} - N_{\mathrm{param}}$ degrees of freedom. We evaluate the localization uncertainty by estimating the 95 per cent-tile of the χ^2 distribution, which is a good approximation of the 95 per cent confidence interval in nonlinear regression when the problem is not strongly nonlinear (Aster *et al.* 2018). The 95 per cent confidence interval is defined by the inequality

$$\chi^2(\mathbf{m}) - \chi^2(\mathbf{m}^*) \leq \Delta^2, \tag{28}$$

where Δ^2 is the 95th percentile of the χ^2 distribution and $\mathbf{m}^*$ the nonlinear least-squares solution. We evaluate Δ^2 such that the probability $P(\chi^2(\mathbf{m}) - \chi^2(\mathbf{m}^*) \leq \Delta^2) = 95$ per cent.

Because the Levenberg–Marquardt method has no guarantee to find the global minimum, especially using BO-TMA and when few sources are used, we carry the inversion multiple times considering different initial guesses close to the *a priori* position of the cable. This strategy significantly improves the chances of convergence towards the true position of the cable.

2.6 Extension to multiple segments

The approach proposed by BO and BF TMA has so far focused on a single fibre segment. The length of this segment must be selected based on the signal-to-noise ratio (SNR), the desired angular resolution and the level of spatial accuracy required. This point will be discussed in more detail in Sections 3.2.2 and 3.2.3, but in practice, the usable segment length typically remains within a few hundred metres at most. To retrieve the geometry of a longer portion of the fibre, it is beneficial to jointly invert multiple adjacent segments. In the following, to enforce geometric coherence between adjacent segments, we introduce a regularization based on two terms: (1) a spatial continuity term ensuring the proper connection of segments, and (2) an angular continuity term promoting smooth orientation changes. Each term is modulated by a specific weight to balance their respective influence in the inversion.

The inversion problem now minimizes the following objective function:

$$\min_{\mathbf{m}} \|\mathbf{d}_{\text{obs}} - \mathbf{G}(\mathbf{m})\|^2 + w_d \|\mathbf{r}_{\text{dist}}\|^2 + w_\gamma \|\mathbf{r}_{\text{azimuth}}\|^2, \tag{29}$$

where $\mathbf{r}_{\text{dist}}$ and $\mathbf{r}_{\text{azimuth}}$ are the residuals associated with the distance and azimuth continuity terms, and w_{d}, w_γ are their respective weights.

To reconstruct the geometry of a fibre that spans several segments, we first extend the inversion scheme to jointly estimate the parameters of all segments. This requires modifying the definition of the state vector, the data vector and the forward operator accordingly.

The full state vector $\mathbf{m} \in \mathbb{R}^{3N_{\text{segments}}}$ now contains the concatenated parameters for all N_{segments} fibre segments. Each segment j is described by its horizontal and vertical coordinates (x_j, y_j) and its azimuth angle γ_j. The full state vector is:

$$\mathbf{m} = \begin{bmatrix} x_1 & y_1 & \gamma_1 & x_2 & y_2 & \gamma_2 & \cdots & x_{N_{\text{segments}}} & y_{N_{\text{segments}}} & \gamma_{N_{\text{segments}}} \end{bmatrix} \in \mathbb{R}^{3N_{\text{segments}}} \tag{30}$$

The observed data vector $\mathbf{d} \in \mathbb{R}^{2N_{\text{obs}}N_{\text{segments}}}$ consists of the pseudo-bearing angles $\theta_{i,j}$ and apparent frequencies $f_{i,j}$ measured at times t_i concatenated for each segment j. It is written as:

$$\mathbf{d} = \begin{bmatrix} \theta_{1,1} & f_{1,1} & \theta_{2,1} & f_{2,1} & \cdots & \theta_{N_{\text{obs}},N_{\text{segments}}} & f_{N_{\text{obs}},N_{\text{segments}}} \end{bmatrix}^\top \in \mathbb{R}^{2N_{\text{obs}}N_{\text{segments}}}. \tag{31}$$

The Jacobian matrix is now of dimension

$$\mathbf{J} \in \mathbb{R}^{2N_{\text{obs}}N_{\text{segments}} \times 3N_{\text{segments}}} \tag{32}$$

and can be described as a block-diagonal matrix. Each block $\mathbf{J}_j \in \mathbb{R}^{2N_{\text{obs}} \times 3}$ corresponds to the contribution of segment j, observations at segment j depend only on its own parameters (x_j, y_j, γ_j). No cross-terms exist between segments in the data misfit part; segments are only coupled via regularization terms, such as continuity or angular smoothness constraints described in the following.

The global Jacobian $\mathbf{J}$ thus takes the block-diagonal form:

$$\mathbf{J} = \begin{bmatrix} \mathbf{J}_1 & \mathbf{0} & \cdots & \mathbf{0} \\ \mathbf{0} & \mathbf{J}_2 & \cdots & \mathbf{0} \\ \vdots & \vdots & \ddots & \vdots \\ \mathbf{0} & \mathbf{0} & \cdots & \mathbf{J}_{N_{\text{segments}}} \end{bmatrix} \in \mathbb{R}^{2N_{\text{obs}}N_{\text{segments}} \times 3N_{\text{segments}}}, \tag{33}$$

where each block $\mathbf{J}_i \in \mathbb{R}^{2N_{\text{obs}} \times 3}$ contains the partial derivatives of the observed angles and frequencies with respect to the parameters (x_j, y_j, γ_j) of the j-th segment.

Now, let us introduce the regularization terms. First, for the spatial continuity terms, we need to define the endpoints as a function of the state parameters. Each segment j is described by its centre position (x_i, y_i) and azimuthal angle γ_i. The segment has a fixed length L, and its endpoints are defined as:

$$\mathbf{x}_j^{(1)} = \begin{bmatrix} x_j \\ y_j \end{bmatrix} - \frac{L}{2}\begin{bmatrix} \sin\gamma_j \\ \cos\gamma_j \end{bmatrix},$$

$$\mathbf{x}_j^{(2)} = \begin{bmatrix} x_j \\ y_j \end{bmatrix} + \frac{L}{2}\begin{bmatrix} \sin\gamma_j \\ \cos\gamma_j \end{bmatrix}.$$

To ensure that the two extremities of segment i and segment $i+1$ align, we define a distance-based regularization residual as:

$$r_j^{\text{dist}} = \left(\left\| \mathbf{x}_{j+1}^{(1)} - \mathbf{x}_j^{(2)} \right\|^2 - d_0^2 \right), \tag{34}$$

where d_0 is the reference separation, typically of the size of the spatial sample of the DAS measurement (here 10 m). This could be put to an arbitrary distance if the segments are not continuous in space, which can happen in case some cable sections are discarded (i.e. low SNR, vibrating segments).

Let define

$$dx = \left(x_{j+1} - \tfrac{L}{2}\sin(\gamma_{j+1})\right) - \left(x_j + \tfrac{L}{2}\sin(\gamma_j)\right), \tag{35}$$

$$dy = \left(y_{j+1} - \tfrac{L}{2}\cos(\gamma_{j+1})\right) - \left(y_j + \tfrac{L}{2}\cos(\gamma_j)\right). \tag{36}$$

Then, the partial derivatives of the continuity residual r_j^{dist} are, relative on the segment j variables

$$\frac{\partial r_j^{\text{dist}}}{\partial x_j} = -2w \cdot \mathrm{d}x, \quad \frac{\partial r_j^{\text{dist}}}{\partial y_j} = -2w \cdot \mathrm{d}y, \quad \frac{\partial r_j^{\text{dist}}}{\partial \gamma_j} = -2w \cdot \left(\mathrm{d}x \cdot \frac{L}{2}\cos(\gamma_j) - \mathrm{d}y \cdot \frac{L}{2}\sin(\gamma_j)\right), \tag{37}$$

and relative to segment $j+1$ variable

$$\frac{\partial r_j^{\text{dist}}}{\partial x_{j+1}} = 2w \cdot \mathrm{d}x, \quad \frac{\partial r_j^{\text{dist}}}{\partial y_{j+1}} = 2w \cdot \mathrm{d}y, \quad \frac{\partial r_j^{\text{dist}}}{\partial \gamma_{j+1}} = 2w \cdot \left(\mathrm{d}x \cdot \frac{L}{2}\cos(\gamma_{j+1}) \cdot \alpha - \mathrm{d}y \cdot \frac{L}{2}\sin(\gamma_{j+1})\right). \tag{38}$$

Let $\texttt{idx\_j} = 3(j-1)$ (i.e. segment j's position in the state vector) the j-th row of the Jacobian J_{dist} is therefore

$$J_{\text{dist}}[j,\ \texttt{idx\_j}+1] = -2w \cdot \mathrm{d}x \tag{39}$$

$$J_{\text{dist}}[j,\ \texttt{idx\_j}+2] = -2w \cdot \mathrm{d}y \tag{40}$$

$$J_{\text{dist}}[j,\ \texttt{idx\_j}+3] = -2w \cdot \left(\mathrm{d}x \cdot \tfrac{L}{2}\cos(\gamma_j) - \mathrm{d}y \cdot \tfrac{L}{2}\sin(\gamma_j)\right) \tag{41}$$

$$J_{\text{dist}}[j,\ \texttt{idx\_j}+4] = +2w \cdot \mathrm{d}x \tag{42}$$

$$J_{\text{dist}}[j,\ \texttt{idx\_j}+5] = +2w \cdot \mathrm{d}y \tag{43}$$

$$J_{\text{dist}}[j,\ \texttt{idx\_j}+6] = +2w \cdot \left(\mathrm{d}x \cdot \tfrac{L}{2}\cos(\gamma_{j+1}) - \mathrm{d}y \cdot \tfrac{L}{2}\sin(\gamma_{j+1})\right) \tag{44}$$

The second regularization term is used to minimize large variations in orientation between segments. We define the angular residual as

$$r_j^{\text{azimuth}} = \begin{cases} \left(\gamma_{i+j} - \gamma_j\right), & \text{if } |\gamma_{j+1} - \gamma_j| > \gamma_{\text{th}}, \\ 0, & \text{otherwise}, \end{cases} \tag{46}$$

where γ_{th} is a threshold (e.g. 5°) beyond which angular continuity is enforced. The j-th row of the Jacobian is therefore

$$J_{\text{azimuth}}[j,\ 3j] = -1, \quad J_{\text{azimuth}}[j,\ 3j+3] = 1 \tag{47}$$

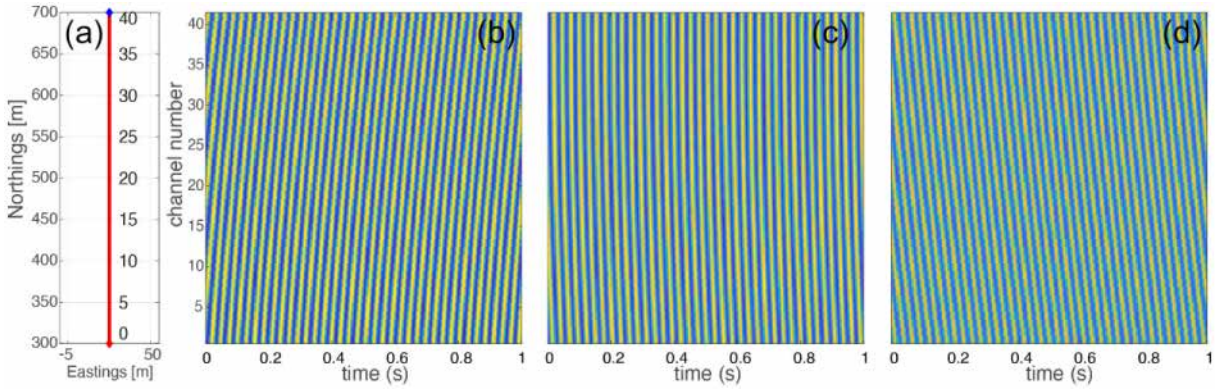

Figure 3. Sample of modelled strain-rate signals generated as the boat moves, recorded by the FO segment. (a) Geometry of the FO segment with channel numbers. The strain-rate signals are shown at three different times: 0 s (b), 90 s (c) and 180 s (d). The vertical axis represents the channel indices along the FO segment.

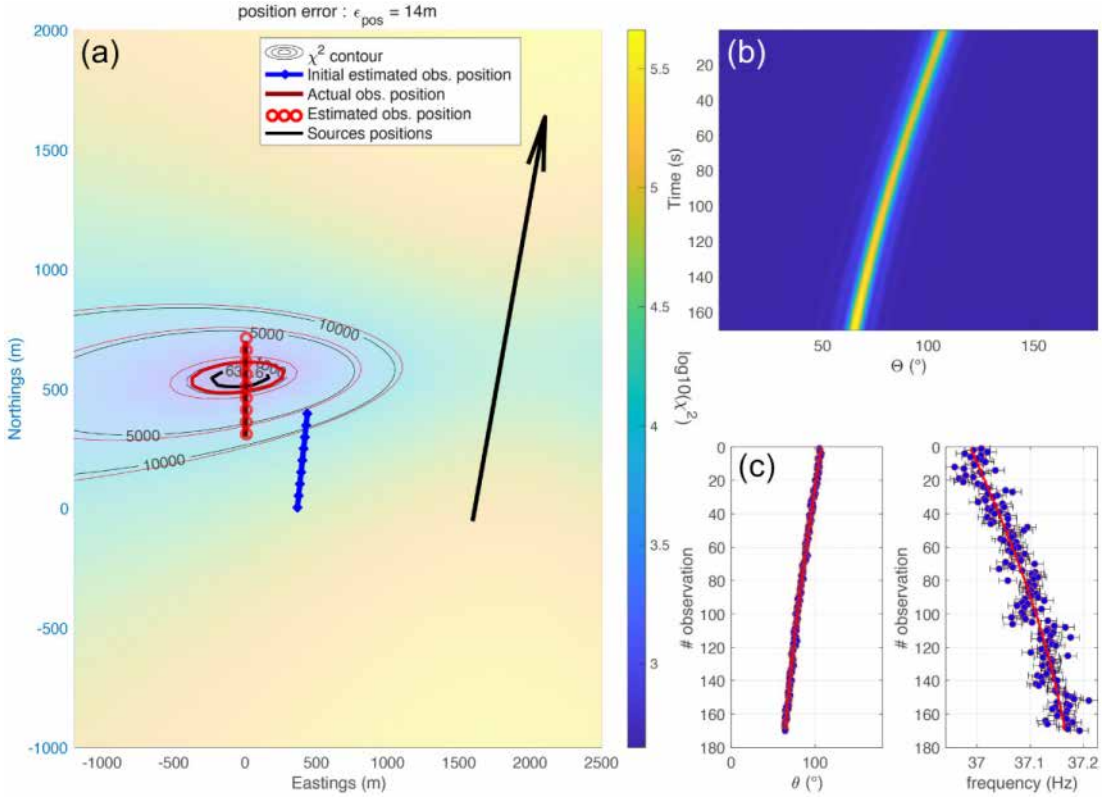

Figure 4. 3-D Bearing and Frequency Target Motion Analysis (BF-TMA) conducted on synthetic data, and comparison of uncertainties between BF-TMA and Bearing-Only Target Motion Analysis (BO-TMA). (a) Map view of the BF-TMA results. A single source was analysed (black arrow). The initial guess of the cable location is shown by the blue segment, the true cable location by the dark red line and the best estimated position by the red circles. The residuals χ^2, represented on a logarithmic scale, are computed on a 2-D spatial grid, with γ_{FO} fixed to the best estimated value from the BF-TMA analysis. Contours of the residual χ^2 values are displayed for both the BF-TMA (black contours) and the BO-TMA analysis (red contours). The bold contour indicates the 95th percentile of the χ^2 distribution, which approximates the 95 per cent confidence interval of the BF-TMA (black) and BO-TMA (red) best estimates of the cable-segment centre position. (b) Beam forming result performed on 30 s time-window sliding every 1 s on the synthetic DAS data for an acoustic source of 37 Hz. (c) Comparison between the measured and modelled pseudo-bearing angles θ shown by blue dots and red line, respectively. (d) Same as (c) but for the frequency. Measurement's noise with a standard deviation of 1° in bearing and 0.016 Hz in frequency was introduced. Pseudo-bearing and frequency were determined using beam forming.

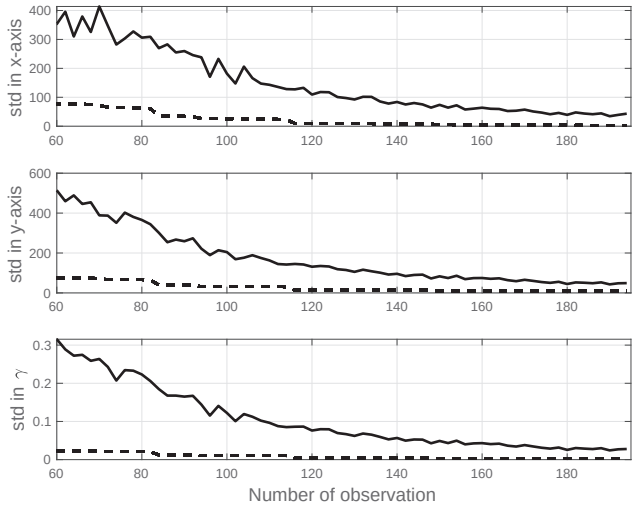

Figure 5. Comparison of the standard deviation of the inverted parameters (blue lines) with the square root of the Cramer-Rao bound (red lines).

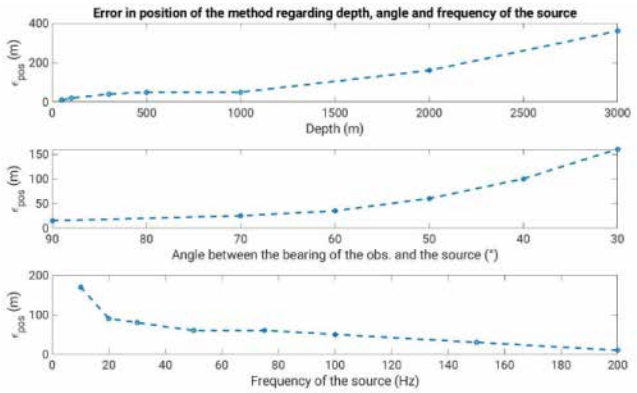

Figure 6. Precision of the solution as a function of depth parameters. For each parameter, the error between the actual position and the estimated position is measured.

The total continuity regularization residual vector is constructed by concatenating all spatial and angular terms:

$$\mathbf{r}_{\text{regularization}} = \left[r_1^{\text{dist}}, \ldots, r_{N_{\text{segments}}}^{\text{dist}}, r_1^{\text{azimuth}}, \ldots, r_{N_{\text{segments}}}^{\text{azimuth}} \right]^T. \tag{48}$$

When adding regularization terms, additional rows appear in $\mathbf{J}$ that couple parameters of neighbouring segments. These introduce off-diagonal blocks, resulting in the augmented Jacobian:

$$\mathbf{J}_{\text{total}} = \begin{bmatrix} \mathbf{J}_{\text{data}} \\ \mathbf{J}_{\text{regularization}} \end{bmatrix}, \tag{49}$$

with

$$\mathbf{J}_{\text{regularization}} = \begin{bmatrix} \mathbf{J}_{\text{dist}} \\ \mathbf{J}_{\text{azimuth}} \end{bmatrix}. \tag{50}$$

This structure allows for joint inversion of multiple segments, enforcing spatial coherence while fitting the observed data.

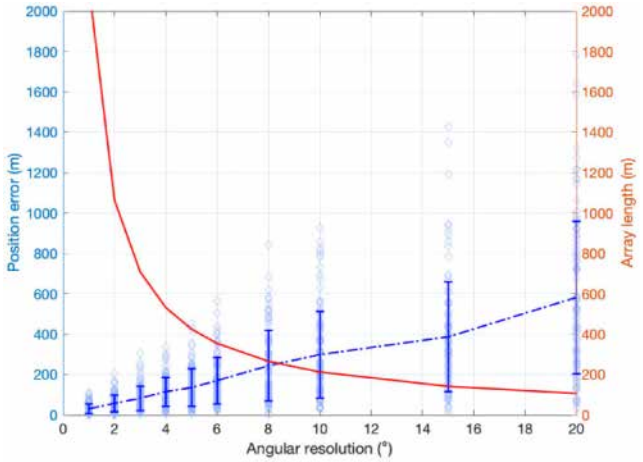

Figure 7. Localization error between the estimated and true positions of the fibre segment as a function of the angular resolution. Each realization is represented by a light blue diamond. Error bars indicate the mean and standard deviation over 100 realizations for each angular resolution. The array length as a function of angular resolution (beamwidth) is shown in red.

3 SYNTHETIC TESTS

3.1 Case study: BF-TMA on synthetic DAS data

We first apply the method to synthetic data, with pseudo-bearing and frequency determined through beamforming. We consider realistic data processing conditions.

Using an analytical acoustic wave simulation code, we simulate strain time-series along the fibre due to an acoustic source passing near the cable. We consider the cosine squared angular sensitivity of DAS, which makes it blind to signals propagating perpendicular to the fibre, and the response $sinc$ due to spatially integrated DAS measurement over the gauge length (Bakku 2015; Hartog 2017). The physical parameters of the seabed and the cable response, such as the coupling between the cable and the ground or the cable Poisson ratio, are not taken into account.

We express the strain-rate for acoustic waves reaching the fibre and detected by DAS in a water layer with constant acoustic wave speed c, following the methodology outlined in Rivet *et al.* (2021). For an incoming acoustic wave with particle velocity A_v, angular frequency ω, wave-number $\vec{k}$, the induced strain along a fibre aligned with the x-axis is

$$\epsilon_{xx} = \frac{-A_v}{c} \cos^2(\theta)\ \exp^{i(\omega t - \vec{k}\cdot\vec{r})}, \tag{51}$$

where θ is the angle between $\vec{k}$ and the x-axis, $\vec{r}$ is the vector between the source and the receiver and t is time. DAS measures strain-rate averaged over a gauge length L_{DAS}, which is:

$$\dot{\epsilon}_{\text{DAS}} = \dot{\epsilon}_{xx}\ \text{sinc}\left(k_x \frac{L_{\text{DAS}}}{2}\right). \tag{52}$$

The Levenberg–Marquardt method requires an initial guess for the cable parameters. In practical cable repositioning applications, a suitable initial guess can be obtained by projecting the path of the vessel that deployed the cable onto the seafloor. In the current example we set $x_{\text{FO}_1} = 400\,\text{m}$, $y_{\text{FO}_1} = 200m$ and $\gamma_{\text{FO}_1} = 0°$, while the real position is $x_{\text{FO}_{\text{true}}} = 0\,\text{m}$, $y_{\text{FO}_{\text{true}}} = 500\,\text{m}$ and $\gamma_{\text{FO}_{\text{true}}} = 15°$. The depth of the cable is 1000 m. The source's coordinates and trajectory are known through AIS positioning.

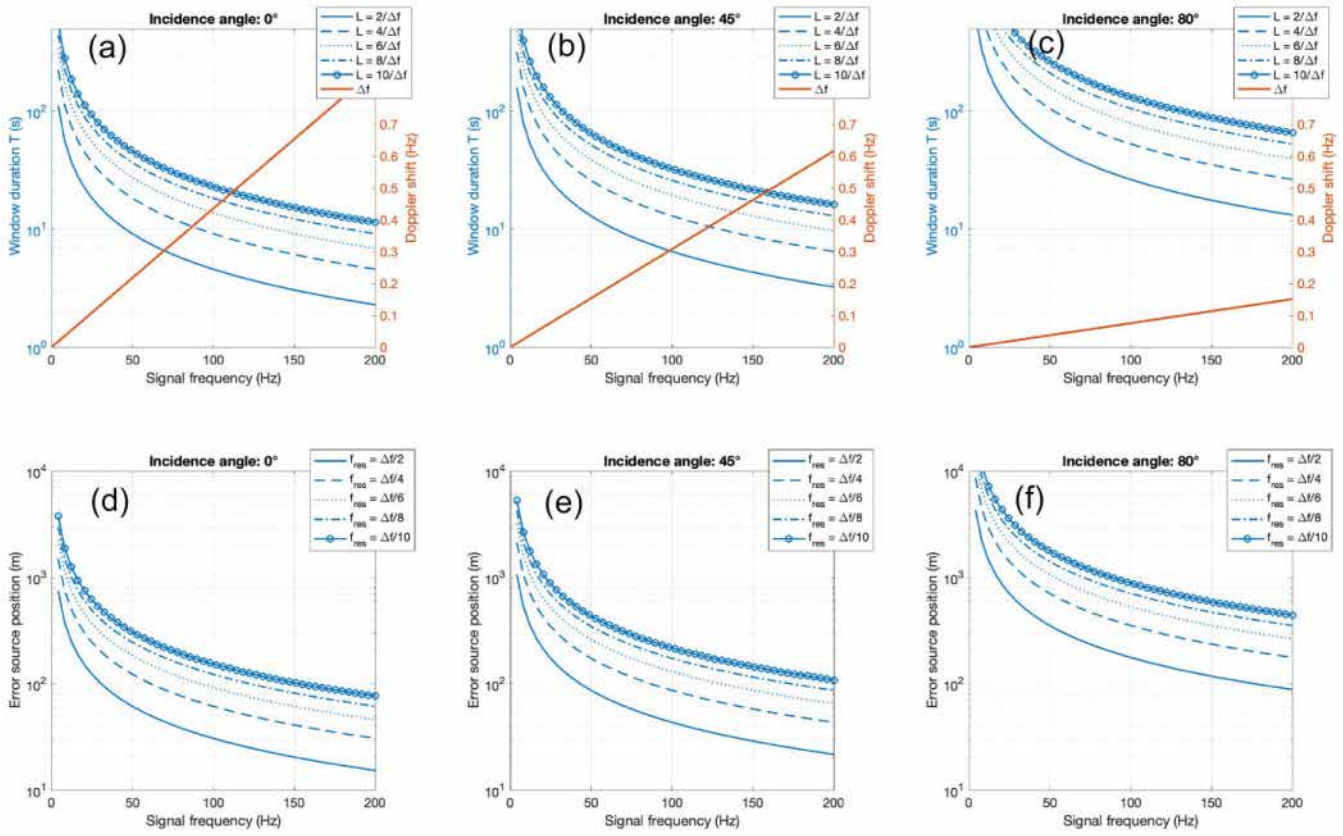

Figure 8. Time window length (a, b and c) and corresponding source position uncertainties (d, e and f) required to resolve the Doppler shift as a function of source frequency, apparent velocity variation and frequency resolution. The red lines correspond to the Doppler.

In this example, $x_{s_0} = 1550\,\text{m}$, $y_{s_0} = -200\,\text{m}$, $v_x = 3\,\text{m}\,\text{s}^{-1}$ and $v_y = 10\,\text{m}\,\text{s}^{-1}$.

Beam forming is applied to a sliding window of 30 s on a 200-s-long signal, using the same temporal sampling as applied to the real data. The antenna used is 410 m long and consists of 41 sensors spaced 10 m apart. Fig. 3 displays a sample of the modelled strain-rate signal over a one-second duration, recorded across all selected channels, at different times as the boat moves.

To measure the pseudo-bearing angle, we pick the maximum energy for each beamforming performed for each time window. In real cases, coherent noise sources may occasionally be more energetic than the targeted source. In such cases, after detrending the polynomial that best fits the angles, we estimate the standard deviation and ignore values beyond 2 times the standard deviation. For frequency measurement, we also do it through the beamforming measurement, which we resolve in frequency. Here, the frequency of the maximum beamformed energy is retained.

We incorporate noise into the pseudo-bearing estimates using a standard deviation of 1°. In acoustic measurements, the beamwidth at the −3 dB level defines the resolution limit and is given by

$$\theta_w = 50\frac{c}{f\,L}, \tag{53}$$

where ff is the frequency, LL is the array length (or aperture), cc is the wave speed and θ_w is expressed in degrees (Medwin & Clay 1997). This beamwidth represents a conservative estimate—an upper bound—on the angular resolution. In our case, for a frequency of 37 Hz, an array length of 410 m, and a sound speed of 1500 $\text{m}\,\text{s}^{-1}$, the beamwidth is approximately 4.9°, corresponding to an angular spread of about ±2.4° around the beam centre. In practice, especially in high signal-to-noise conditions, the actual angular error obtained from peak-picking is typically significantly smaller than the beamwidth. Based on our tests on real data, we adopt a standard deviation of 1° for the pseudo-bearing uncertainty, which realistically reflects the observed variability in beamforming results.

The frequency measurement uncertainty depends on the frequency resolution in the beamforming calculation, which is equal to the reciprocal of the window length. Here, we assume a standard deviation of 0.16 Hz, which is half the frequency resolution.

The result of 3-D BF-TMA applied to synthetic data is shown in Fig. 4. The $\chi^2(m)$ values are computed for x_{FO} ranging from −1200 to 2500 m and for y_{FO} ranging from −2000 to 2500 m, with increments of 100 m, fixing γ_{FO} at it best estimated value. The bold contour shown in the figure represents the 95 per cent-tile of the χ^2 distribution. The *a posteriori* error is of only 18 m in this example, but the 95 per cent confidence interval covers an area of several hundred meters in the less constrained direction (x-axis). This confidence interval can be further reduced by incorporating additional source trajectories recorded by the fibre optical cable on different experiments, as will be shown later in Section 4, with an example of relocation using multiple sources. The cable's positioning can thus be further improved with future experiments recording more boats.

The convergence of the algorithm on this simple synthetic test that mimics a real case study validates the idea that the method can be applied to real data. This method is well-suited for relocating a fibre optic cable.

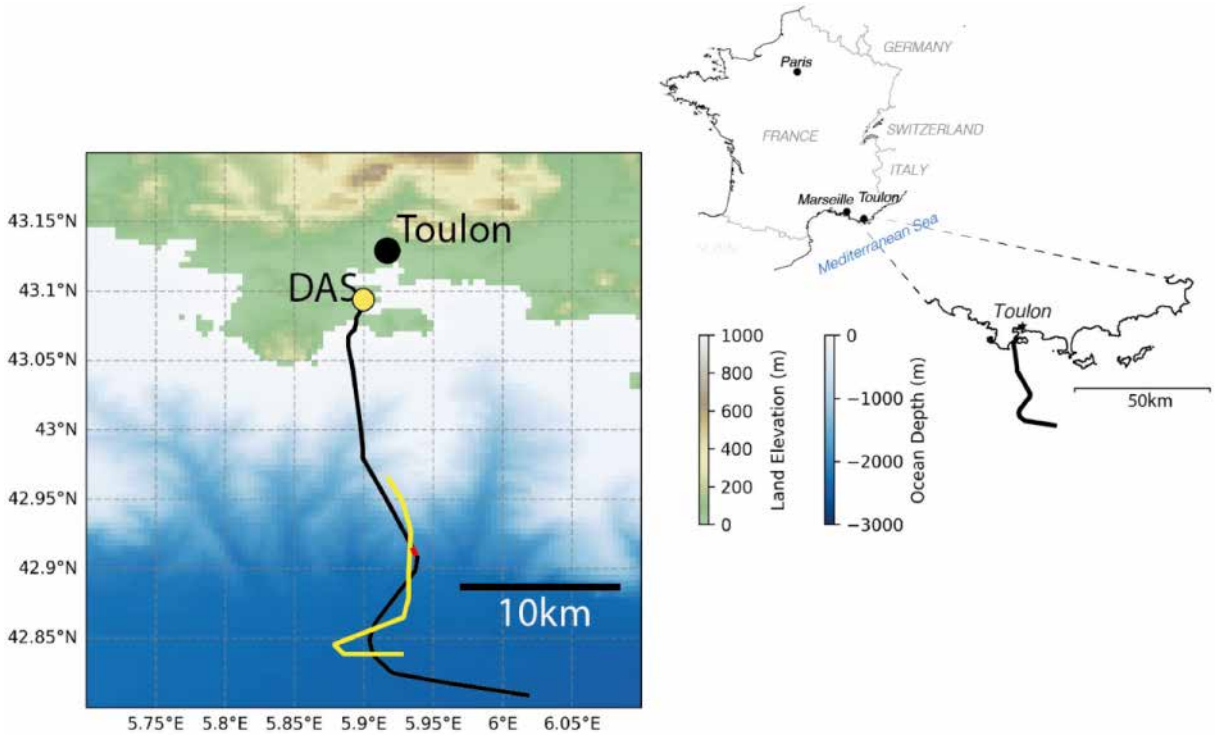

Figure 9. Cable position (black line) and boat trajectory (yellow line) in a real configuration. The red section corresponds to the cable to be relocated.

3.2 Performance of 3-D BF-TMA

3.2.1 Quantifying estimation accuracy using the Cramér-Rao bound

To quantify the performance of this algorithm, we compare the variance of our estimator, applied to synthetic data with noise, to the Cramer-Rao bound (CRB), which is defined as the variance of an ideal unbiased estimator and is given by the inverse of the Fisher information matrix. This bound provides a theoretical lower limit on the variance of our estimator. The calculations can be found in Nardone *et al.* (1984), Le Cadre *et al.* (2000) and Ho & Chan (2006b).

In this synthetic exercise, using the same geometry as in Fig. 4, the total number of observations is increased to 195. This means that the source trajectory contains up to 195 positions, and the boat is observed for 3.25 min. We performed a statistical study on 200 draws, starting with a subset of 60 observations (1 min long) and increasing up to 195 observations. Pseudo-bearing and frequency values were determined through beam forming. The standard deviation of the estimated parameters x_{FO}, y_{FO} and γ_{FO} was compared to the CRB, which is displayed here as $\sqrt{\mathrm{CRB}}$ (Fig. 5). The CRB is reached asymptotically, demonstrating the efficiency of the algorithm.

We then analyse how the precision of the solution is affected by the FO depth, source frequency and the source angle relative to the fibre (Fig. 6). The results of this analysis can help us optimize the selection of sources for relocating the cable. The convergence of the method is even more assured when the Doppler shift in frequency (i.e. projected velocity) is greater, which according to the eq. (8) corresponds to high frequency or shallow depth. As we move away from these optimal conditions, frequency extraction by the beam forming method may lose accuracy. Under these conditions, the estimation of the observer's position is less reliable. The optimal angle between the FO and the source being around the broadside of the cable, we observe that the error increases when the angle between the source and the observer is less than 50°. However, due to the angular sensitivity of the cable, detecting boats close to the vertical may be challenging (Mateeva *et al.* 2014b). Boats detected at angles around 60°, where sensitivity is sufficient (Rivet *et al.* 2021), represent a good compromise between beam forming accuracy and signal-to-noise ratio.

3.2.2 Evaluating the trade-off between angular and spatial resolution

In beam forming-based relocation, a fundamental trade-off arises between angular resolution and spatial resolution.

On the one hand, short segments improve spatial accuracy and ensure that each estimated source position reflects local variations along the fibre. On the other hand, angular resolution depends strongly on the effective aperture length L relative to the wavelength λ as stated in eq. (53). Thus, longer segments are required to reduce the uncertainty in the direction of arrival.

This trade-off implies that high spatial resolution (short L) comes at the cost of poor angular resolution, while long segments improve beam forming performance but reduce the ability to localize spatial variations along the array.

As a practical example, we consider that a boat emits at a frequency of 36 Hz, and we estimate the average localization error of a fibre segment as a function of the angular resolution (beamwidth). We make a conservative assumption that the angular measurement error is equal to half the beamwidth, which can indeed occur in cases of very low signal-to-noise ratio (SNR). These estimates are compared over different array lengths L (Fig. 7). We find that a good compromise between spatial and angular resolution is obtained for $L \approx 265$ m, which corresponds to a beamwidth of approximately

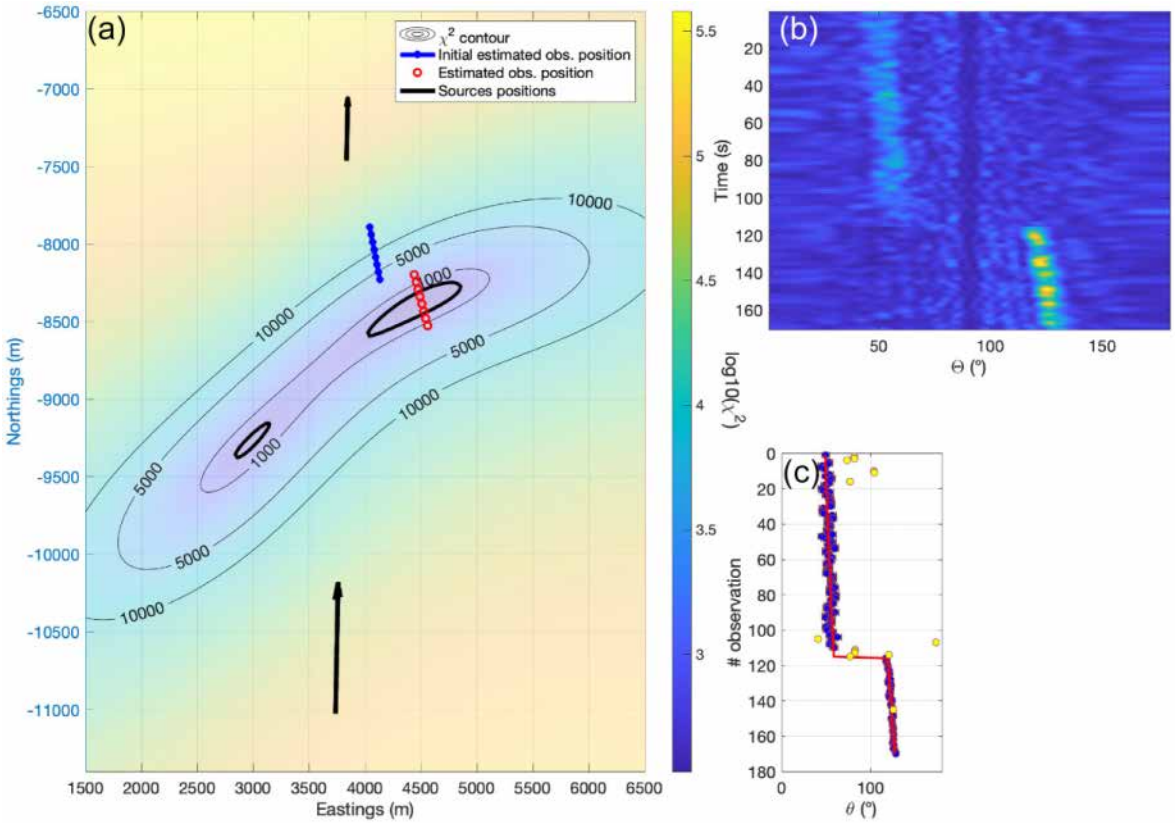

Figure 10. 3-D Bearing-Only Target Motion Analysis (BO-TMA) conducted on real data. (a) A 2-D map of the BO-TMA results. Two different sources from a single boat at two different times period were analysed (black arrows). The initial guess of the cable location is indicated by the blue segment, the best estimate of the position by the red circles. The residuals, χ^2, represented on a logarithmic scale, are computed on a 2-D spatial grid, fixing γ_{FO} to the best estimated value from the BO-TMA analysis. Contours of χ^2 are displayed. The bold contour indicates the 95-th percentile of the χ^2 distribution, which approximates the 95 per cent confidence interval for the BO-TMA best fibre position. (b) Beam forming results performed on a 6-s time window sliding every 1 s on the DAS synthesized data for an acoustic source of 37 Hz. (c) Comparison between the measured and modeled pseudo-bearing angles θ, shown by blue dots and the red line, respectively. Pseudo-bearing angles outside the 1.5-sigma are considered as outliers and not included in the inversion (yellow dots).

8° and a normalized aperture $N = L/\lambda \approx 6.2$, with acceptable performance for N in the range of 5.5–7.

3.2.3 Doppler resolution and its implications

For the Doppler shift data to be informative, it must be sufficiently well-resolved. The Doppler shift depends on the apparent velocity—it is maximal when the boat is moving directly toward or away from the sensor, along the axis defined between the fibre and the boat—and on the source frequency, with higher frequencies yielding greater shifts. We define the Doppler frequency difference, reformulated from eq. (5), as

$$\Delta f = f_d - f_s = \frac{v_s \cos(\theta)}{c_0} f_s \tag{54}$$

with θ the angle of incidence between the direction of motion of the boat and the axis defined between the fibre and the boat.

To resolve the Doppler difference Δf, the frequency resolution f_{res} of the beamforming analysis must be smaller than $\Delta f/2$. We can express the frequency resolution and time window length for beam forming as T,

$$f_{\text{res}} \leq \frac{\Delta f}{k} \quad \Rightarrow \quad T \geq \frac{k}{\Delta f}, \tag{55}$$

where k is a resolution factor (the higher the value, the better the resolution). The minimal requirement to resolve the Doppler shift is met with $k = 2$.

The time window T required to resolve the frequency difference directly translates into an uncertainties in the source position, due to the vessel's displacement during T, $\varepsilon_{\text{source}} = T \times v$. There is a trade-off between the precise resolution of the Doppler shift, which is required to achieve precise relocation of the fibre, and the spatial resolution that can be achieved for a given time window length.

Fig. 8 displays time window length and the corresponding spatial resolution of the source position, required to resolve the Doppler difference, as a function of source frequency and apparent velocity. Here we consider the average tankers' speed at approximately 13 knots (24 km h^{-1})—which are likely to generate DAS signals with a signal-to-noise ratio above 3 dB—travel. We see that higher frequencies should be targeted to be included in the inversion, as they can resolve the source position with sufficiently small errors and achieve fine frequency resolution.

3.3 Case study: 3-D bearing-only target motion analysis

When the configuration is not optimal for the use of the Doppler shift as seen in previous section, a frequency shift may be difficult to measure with sufficient precision. We investigate the possibility to apply the 3-D BO-TMA algorithm, based on pseudo-bearing alone,

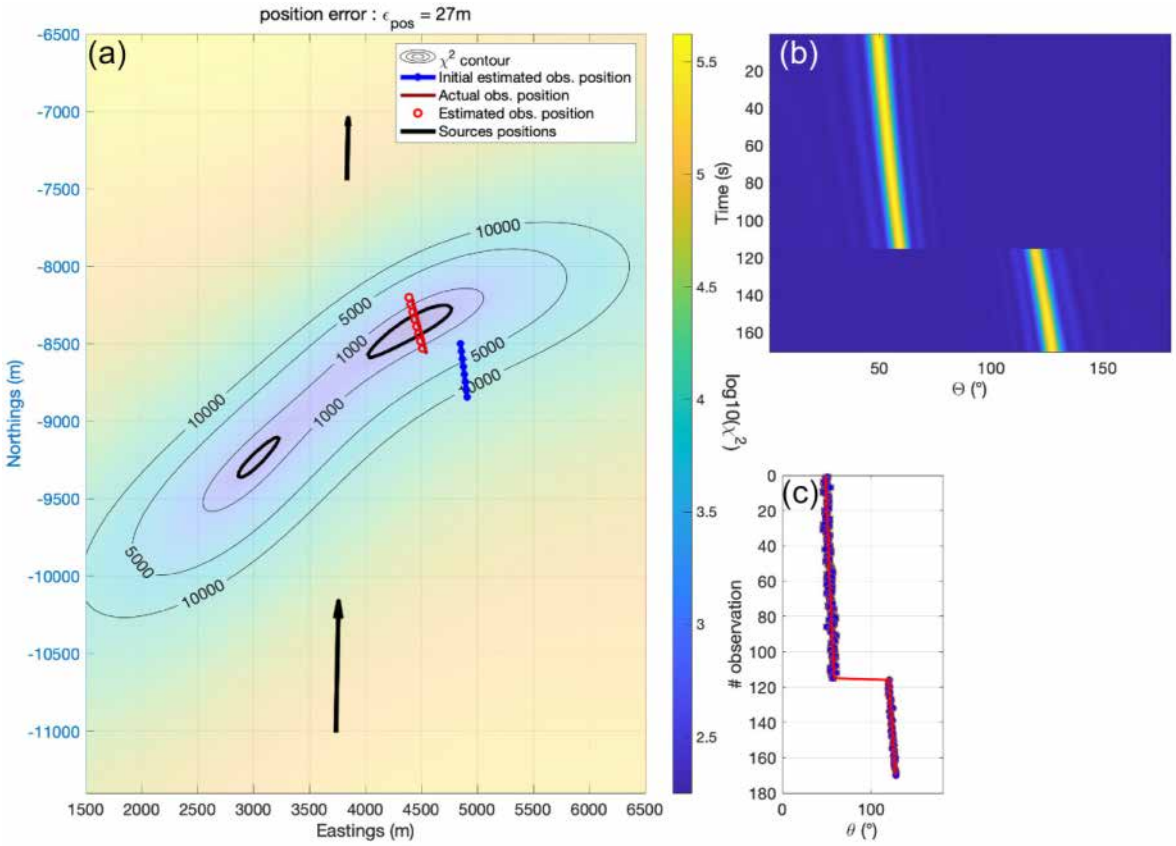

Figure 11. Same as Fig. 10. BO-TMA conducted on synthetic data with a geometry close to the experiment we conducted in Toulon. A total of four boat trajectories were used in the inversion. Measurement's noise with a standard deviation of 1° in bearing were introduced for the third and fourth UMR transits of the source.

to one or multiple sources in URM. Unlike BO-TMA, which is used to track a moving source from a stationary observer and results in an infinite number of possible solutions (due to the position ambiguity along a hyperbola), in our case, the boat's speed is known. This knowledge eliminates the distance ambiguity, constraining the inversion process even when only the pseudo-bearing is utilized. Fig. 4 shows in dark red the residual that would be obtained for BO-TMA case, with only the bearing angle being inverted. The confidence interval is slightly larger, as the Doppler frequency shift is well resolved in the previous case. This result demonstrates that BO-TMA can serve as a viable alternative when frequency measurements are not sufficiently accurate.

4 APPLICATION TO REAL DAS DATA

Based on the DAS data we have explored, the measurement and use of pseudo-bearing alone proved to be sufficiently robust. Consequently, we adopt a Bearing-Only Target Motion Analysis (BO-TMA) approach. We apply it to the strain rate time-series recorded in July 2020 on a 42 km-long underwater fibre optic cable deployed off the coast of Toulon, south-east France. This KM3NeT-Fr infrastructure is part of the MEUST (Mediterranean Eurocentre for Underwater Sciences and Technologies) and NUMerEnv (NeUtrino Mer Environment) projects (Lamare 2016; Coyle *et al.* 2017). An Aragon Photonics HDAS interrogator unit was connected to one end of the fibre. During the DAS acquisition, an 80-m-long and 20-m-wide vessel sailed above the cable, and its AIS position was recorded with an average temporal resolution of 3 min.

In this acquisition, the spatial sampling (distance between two sensing points) is set at 10 m, and the gauge length at 20 m and temporal sampling is set at 1 KHz. We selected a section of cable to be relocated that is 21 km from the interrogator unit along the fibre (Fig. 9). The section of cable studied consists of 40 sensors, resulting in an antenna length of 400 m. This section was chosen because it is linear; despite the uncertainty regarding the exact position of the cable, it can be assumed to be rectilinear over this distance. This linearity is necessary for applying the 3-D BO-TMA method developed here. Additionally, the signal recorded on this section, unlike other sections, has a high signal-to-noise ratio, enabling the exploitation of two boat segments and the measurement of pseudo-bearing angles. The two signal sequences studied last 120 and 60 s, respectively. The sliding time windows used for beam forming are set at 30 s, ensuring the source's position remains accurately known. By recording one pseudo-bearing observation per second, we gathered two data sets with 115 and 55 observations each.

Fig. 10 displays the inversion result using BO-TMA. In this case, the two independent URM sections of the source are studied simultaneously. The standard deviation of each individual pseudo-bearing angle was estimated independently for each lag. Outlier pseudo-bearing angles exceeding 1.5 times the standard deviation were assigned a large error and thus neglected in the inversion (indicated by the yellow dots in Fig. 10c). While the angles between the source positions and the source are quite far from the broadside, the pseudo-bearing angles remain below 60°, ensuring observability.

We performed a synthetic test, illustrated in Fig. 11, to replicate the configuration of the real-case experiment. The synthetic data

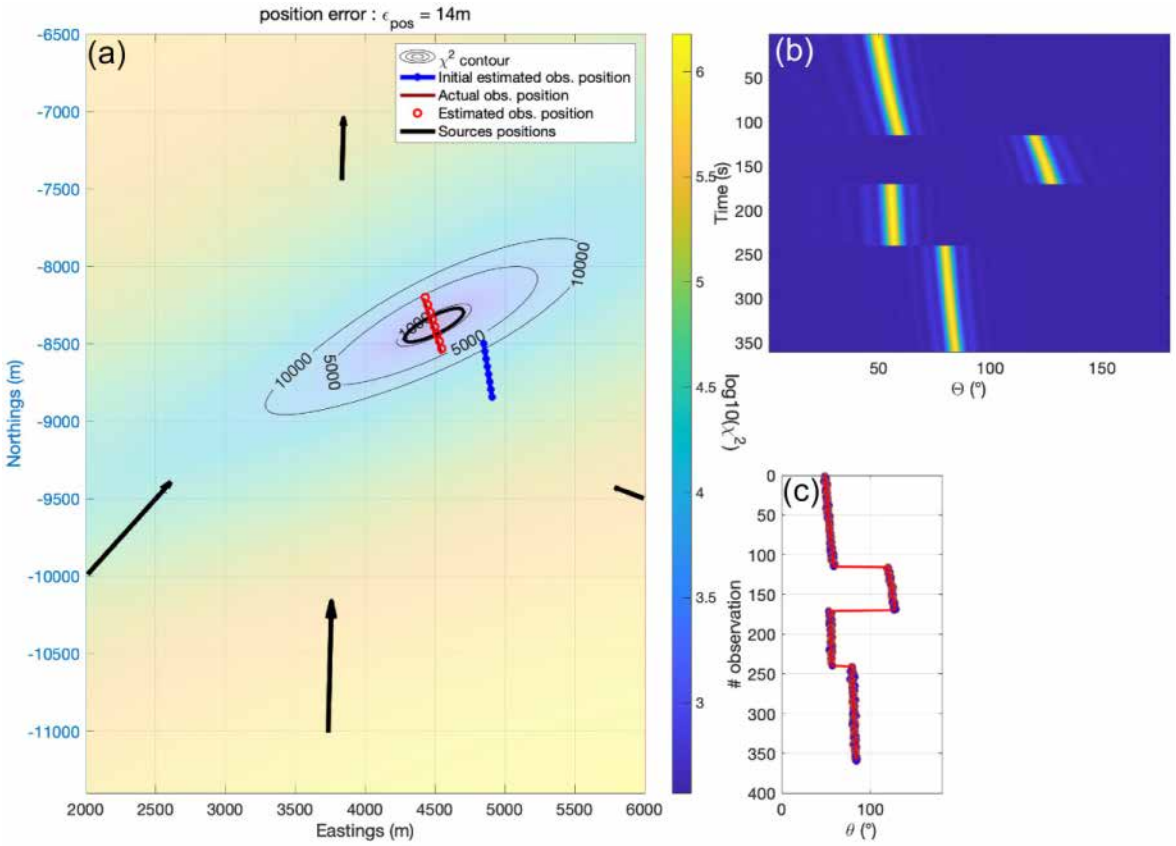

Figure 12. Same as Fig. 10. BO-TMA conducted on synthetic data with a geometry close to the experiment we conducted in Toulon. Measurement's noise with a standard deviation of 1° in bearing were introduced for all the UMR transits of the source.

simulate the DAS strain rate time-series measured at a fibre segment positioned at the location estimated by the BO-TMA inversion. The results of this test are consistent, showing two lobes of possible positions within a 95 per cent confidence interval.

This initial synthetic test enabled us to further evaluate the impact of incorporating multiple source paths, as shown in Fig. 12. Here, we added two additional boat trajectories, maintaining the source frequency at 37 Hz, with the boats travelling at velocities of 13 and 6 knots, respectively. The localization uncertainties are significantly reduced, resulting in a single lobe.

Finally, we investigate a case study demonstrating the extension of the relocation method to multiple segments, using synthetic data that mimic the configuration of the real experiment. Building on the previous multisource relocation—which represents a more favourable scenario—we now apply the multisegment relocation approach described in Section 2.6 using BF-TMA (Fig. 13). For each segment, we assume that the same sources are visible; however, the method is compatible with varying source visibility, which is expected in very long fibre deployments. In this example, we consider four segments, each 390 m in length. The initial configuration is offset by 10° in azimuth, 300 m in longitude and –400 m in latitude. We retrieve position errors of less than 30 m, which are within an acceptable range compared to the uncertainties expected for a single segment, shown by the 95 per cent confidence interval in Fig. 12. We observe that the continuity regularization ensures even distances between segments, while the azimuth regularization provides smooth changes in azimuth.

5 DISCUSSION

The TMA methods presented here enable the real position of an underwater fibre optic cable segment to be determined, based on an initial estimate. This is achieved using either a combination of pseudo-bearing and frequency data or pseudo-bearing data alone, recorded over several observations of acoustic waves from a moving source. While the results presented here are based on a single source and achieve a relocation precision within 100 m, the performance of the method can be greatly improved by including more sources as shown in Fig. 12. Doppler shift observations can be used to further constrain the solution. However, as seen in Section 3.2.3, the shift can be very small and difficult to measure for low-frequency sources (< 100 Hz).

Currently, the method only inverts for the position and azimuth of linear portions of cable. With improved localization, other parameters related to the bathymetry, which are assumed to be known here, may also need to be inverted.

Here, the slope of the cable was assumed to be zero. For the section of cable studied, the slope is likely less than 5°. This approximation interferes with the algorithm's estimation of the cable's position. To account for this, we first need to redefine the pseudo-bearing misfit we are trying to minimize, then integrate it into the calculation of the Jacobian matrix. The state vector would then become $\mu = (x_{\mathrm{FO}}, y_{\mathrm{FO}}, \gamma_{\mathrm{FO}}, \psi_{\mathrm{FO}})$, where ψ_{FO} is the slope of the cable. However, considering a slope of 5° will lead to an error of 87 m at a depth of 1000 m, which is within the uncertainties of the best location estimation when considering a single source.

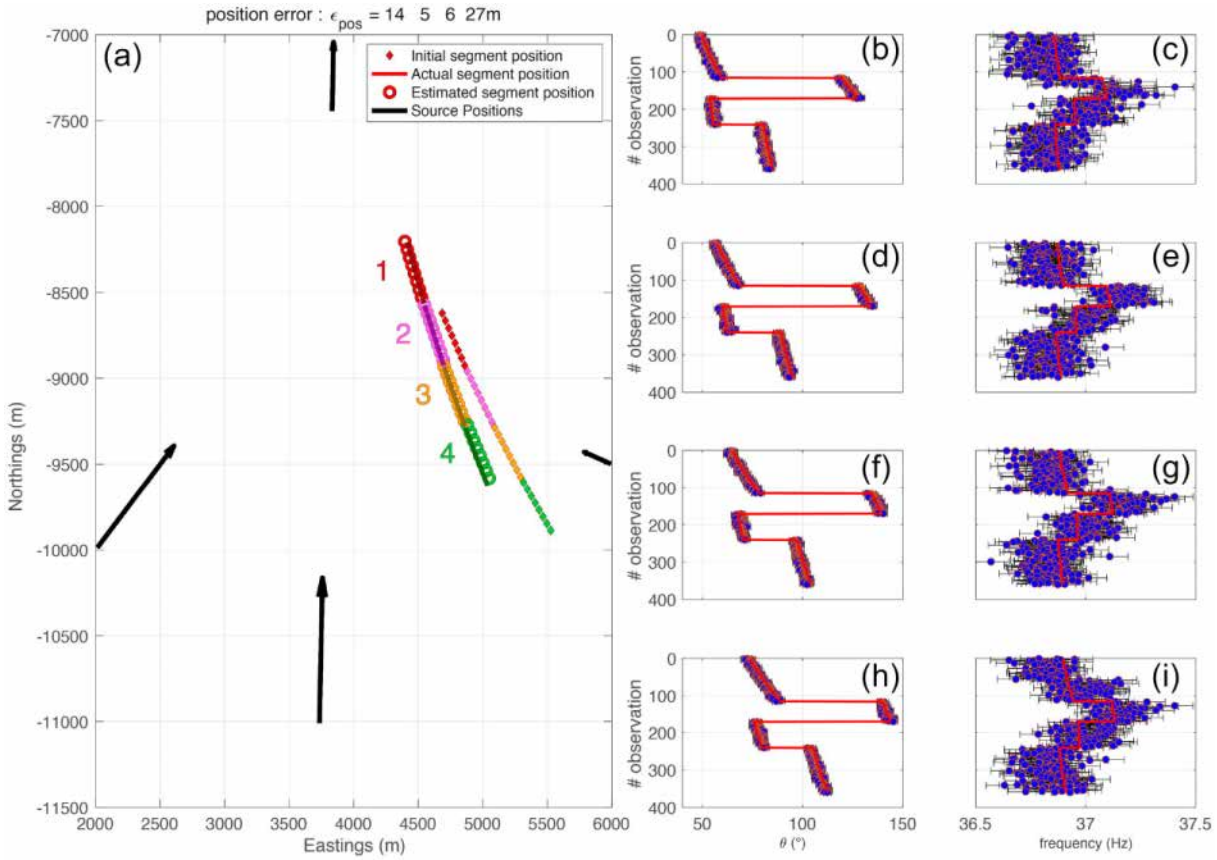

Figure 13. BF-TMA performed on synthetic data for four fibre segments, using a geometry similar to the real experiment conducted off Toulon. Four distinct boat UMR transits were used in the inversion. (a) Map view showing the initial guess, actual and estimated segment positions. The position errors of the four segments are indicated in the title. (b,d,f,h) For each segment, comparison between the measured and modelled pseudo-bearing angles θ shown by blue dots and red line, respectively. (c,e,g,i) Same as (c) comparison between the measured frequencies. Measurement's noise with a standard deviation of 1° in bearing and 0.016 Hz in frequency was introduced.

Another parameter that can improve relocation accuracy is the depth of the cable. In our method, the depth is fixed and assumed to be known from the preliminary estimate of the cable geometry. It is conceivable to add the depth as a state parameter and estimate it as well. However, this could affect the observability of the problem. To address this, we could discretize the solution field, using known bathymetry to assign a depth with each longitude/latitude pair. In this way, the algorithm will only propose a solution at one of the depths defined by the bathymetry.

Uncertainties on the sound speed in the water column may as well impact the precision of the relocation. The water column velocity is considered constant here. However, because the sources we typically sense using DAS are located close to the vertical of the fibre, with a maximum sensitivity at 60° from the horizontal (Rivet *et al.* 2021), and because we focus on the direct path, we do not expect the effect to be larger than a few metres.

Finally, when considering large ships, which are typically the noisiest vessels, we assume that the source is co-located with the position of the AIS. This assumption holds true within a few tens of metres, given the distance between the engine and the positioning system on the boat.

While the Levenberg–Marquardt method does not guarantee reaching the global minimum, it does offer advantages. With just three parameters to determine for each fibre segment, global optimization methods prove highly effective and efficient. However, when employing this approach to solve for multiple consecutive fibre segments simultaneously the number of model parameters can substantially rise, making it less suitable for global optimization methods. Moreover, it is not always feasible to invert for the entire cable, and it may be beneficial to invert for segments independently. This was evident in the KM3NeT-Fr cable, where due to site and coupling conditions, a specific acoustic source might not be detected on all cable segments. To ensure finding the global minimum, several starting conditions could be tested around the best-known position.

6 CONCLUSION

We have introduced a method for relocating a straight segment of underwater optical fibre cable using noise emitted by passing ships and recorded on the strain-rate time-series acquired through DAS technology. After outlining the principle of target motion analysis for source localization, we adapted this method for 3-D localization. Given that the inverse problem is not linear, we utilized the Levenberg–Marquardt algorithm to solve it.

Considering a single source, the confidence interval of 95 per cent of the recovered position is about a few hundred metres, depending on the geometry of the source and the fibre. In synthetic tests, the localization is recovered with an accuracy of less than 100 m. This improvement is significant compared to the very sparse location data provided by cable operators. Further enhancement in localization can be achieved by incorporating more sources (AIS

data are publicly available) and conducting longer DAS experiments.

We demonstrate that while a method exploiting pseudo-bearing and frequency simultaneously can help better constrain the location of the cable, it may not always be possible to precisely measure the frequency within ± 0.1 Hz at low frequencies in real data. Another approach exploiting only pseudo-bearing allows for cable relocation within acceptable precision.

This initial implementation establishes a high-performance method for relocating a single section of optical fibre. We have extended the approach to support multiple-segment relocation by introducing a regularization scheme into the Levenberg–Marquardt algorithm. This regularization imposes spatial and angular continuity constraints between adjacent segments, ensuring a coherent reconstruction of the fibre geometry. While the method shows promising results on synthetic data sets, further testing on a broader range of scenarios is needed. In particular, real-data processing components—including the beam forming technique and frequency estimation method—must be further validated and potentially refined. Future efforts will focus on applying this approach to larger fibre sections, with the ultimate goal of enabling relocation of an entire fibre-optic cable network.

ACKNOWLEDGMENTS

DR and JPA are supported by the European Research Council (ERC) under the European Union's Horizon 2020 research and innovation program (grant agreement No. 101041092–ABYSS). The work of Lucas Popotto was funded by a fellowship of Thales DMS S.A. The MEUST-NUMerEnv project is sponsored by CNRSIN2P3, the Region Sud, France (CPER), the State (DRRT), and the Europe (FEDER).

DATA AVAILABILITY

The codes and data used in this study are subject to confidentiality agreements with our industrial partner, Thales SA. As such, the synthetic DAS data generation code and the observed DAS data cannot be publicly shared.

However, all the details necessary to reproduce the key methodological components of the study are fully described in the manuscript. This includes the beam forming step, implemented using a classical frequency-domain approach, and the source inversion procedure, based on a Gauss–Newton algorithm with Levenberg–Marquardt (LM) regularization. The mathematical formulations, including the error functions and Jacobians, are explicitly provided, allowing readers to implement the method independently using standard numerical tools.

DAS data measured on the underwater fibre cable for a specific boat, as presented in this article, cannot be publicly shared due to confidentiality agreements with industrial partners.

Synthetic data used to evaluate the performance of the algorithm presented here will be shared upon request to the corresponding author.

REFERENCES

Andres, J.M., 1998. Real-time controls aid seismic survey cable deployment and retrieval, *Offshore Magaz.*, https://www.offshore-mag.com/subsea/article/16756512/real-time-controls-aid-seismic-survey-cable-deployment-and-retrieval. Accessed: 2025-09-09.

Ashry, I., Mao, Y., Wang, B., Hveding, F., Bukhamsin, A.Y., Ng, T.K. & Ooi, B.S., 2022. A review of distributed fiber–optic sensing in the oil and gas industry, *J. Lightwave Technol.*, **40**(5), 1407–1431.

Aster, R.C., Borchers, B. & Thurber, C.H., 2018. *Parameter Estimation and Inverse Problems*, Elsevier.

Bakku, S.K., 2015. *Fracture Characterization from Seismic Measurements in a Borehole*, Ph.D. thesis, Massachusetts Institute of Technology.

Biondi, E., Wang, X., Williams, E.F. & Zhan, Z., 2023a. Geolocalization of large-scale DAS channels using a GPS-tracked moving vehicle, *Seismol. Soc. Am.*, **94**(1), 318–330.

Biondi, E., Zhu, W., Li, J., Williams, E.F. & Zhan, Z., 2023b. An upper-crust lid over the long valley magma chamber, *Sci. Adv.*, **9**(42), eadi9878.

Boué, P., Roux, P., Campillo, M. & de Cacqueray, B., 2013. Double beamforming processing in a seismic prospecting context, *Geophysics*, **78**(3), V101–V108.

Bouffaut, L.. *et al.*, 2022. Eavesdropping at the speed of light: distributed acoustic sensing of baleen whales in the arctic, *Front. Mar. Sci.*, **9,** 901348.

Brenne, J.K. *et al.*, 2024. Non-intrusive DAS coexisting in telecom networks, in *Optical Fiber Communication Conference*, pp. M4E–3, Optica Publishing Group.

Chan, Y. & Rudnicki, S., 1992. Bearings-only and Doppler-bearing tracking using instrumental variables, *IEEE Trans. Aerospace Electron. Syst.*, **28**(4), 1076–1083.

Cox, H., Zeskind, R. & Owen, M., 1987. Robust adaptive beamforming, *IEEE Trans. Acoust. Speech Signal Process.*, **35**(10), 1365–1376.

Coyle, P., Collaboration K. *et al.*, 2017. KM3NET-ORCA: oscillation research with cosmics in the abyss, *J. Phys.: Conf. Ser.*, **888**(1), 012024.

Daley, T.M.. *et al.*, 2013. Field testing of fiber-optic distributed acoustic sensing (das) for subsurface seismic monitoring, *Leading Edge*, **32**(6), 699–706.

Dou, S. *et al.*, 2017. Distributed acoustic sensing for seismic monitoring of the near surface: a traffic-noise interferometry case study, *Sci. Rep.*, **7**(1), 11620.

Ferguson, E.L., Williams, S.B. & Jin, C.T., 2019. *CASSP 2019 - 2019 IEEE International Conference on Acoustics, Speech and Signal Processing (ICASSP)*, pp. 551–555, Brighton, UK.

Fernández-Ruiz, M.R. *et al.*, 2022. Seismic monitoring with distributed acoustic sensing from the near-surface to the deep oceans, *J. Lightwave Technol.*, **40**(5), 1453–1463.

Gao, Y., Clark, M. & Cooper, P., 2008. Time delay estimate using cepstrum analysis in a shallow littoral environment, *in Proceedings of the 3B.3 UDT Europe, Glasgow UK*, Vol. **7,** p. 8.

Gazzah, H. & Marcos, S., 2005. Cramer-Rao bounds for antenna array design, *IEEE Trans. Signal Process.*, **54**(1), 336–345.

Gemba, K.L., Sarkar, J., Cornuelle, B., Hodgkiss, W.S. & Kuperman, W., 2018. Estimating relative channel impulse responses from ships of opportunity in a shallow water environment, *J. Acoust. Soc. Am.*, **144**(3), 1231–1244.

Gera, G.P. & Mulgrew, B., 2009. Antenna array cramer-rao bound design by element relocation, in *2009 17th European Signal Processing Conference*, pp. 1141–1145, IEEE Glasgow, UK, 2009.

Guerin, G., Rivet, D., van den Ende, M., Stutzmann, E., Sladen, A. & Ampuero, J.-P., 2022. Quantifying microseismic noise generation from coastal reflection of gravity waves recorded by seafloor das, *Geophys. J. Int.*, **231**(1), 394–407.

Hartog, A.H., 2017. *An Introduction to Distributed Optical Fibre Sensors*, CRC Press.

Ho, K. & Chan, Y.T., 2006a. An asymptotically unbiased estimator for bearings-only and Doppler-bearing target motion analysis, *IEEE Trans. Signal Process.*, **54**(3), 809–822.

Ho, K. & Chan, Y.T., 2006b. An asymptotically unbiased estimator for bearings-only and Doppler-bearing target motion analysis, *IEEE Trans. Signal Process.*, **54**(3), 809–822.

Jousset, P. *et al.*, 2018. Dynamic strain determination using fibre-optic cables allows imaging of seismological and structural features, *Nat. Commun.*, **9**(1), 2509.

Lamare, P., 2016. The MEUST deep sea infrastructure in the Toulon site, in *EPJ Web of Conferences*, Vol. **116,** p. 5, EDP Sciences .

Landrø, M. *et al.*, 2022. Sensing whales, storms, ships and earthquakes using an arctic fibre optic cable, *Sci. Rep.,* **12**(1), 19226.

Le Cadre, J.-P., Gauvrit, H. & Trarieux, F., 2000. Approximations of the Cramér–Rao bound for multiple-target motion analysis, *IEE Proc.-Radar Sonar Navigation,* **147**(3), 105–113.

Lindsey, N.J., Dawe, T.C. & Ajo-Franklin, J.B., 2019. Illuminating seafloor faults and ocean dynamics with dark fiber distributed acoustic sensing, *Science,* **366**(6469), 1103–1107.

Lior, I. *et al.*, 2021. On the detection capabilities of underwater distributed acoustic sensing, *J. geophys. Res.: Solid Earth,* **126**(3), e2020JB020925.

Mamatsopoulos, V.A., Michailides, C., Theotokoglou, E.E. & Onoufriou, T., 2020. Critical water depth and installation curves for submarine cable deployment process, *J. Mar. Sci. Eng.,* **8**(11).

Mata Flores, D., A., Sladen,, Ampuero, J.-P., Mercerat, D. & Rivet, D., 2023. Monitoring deep Sea currents with seafloor distributed acoustic sensing. , in *Earth and Space Science,*, Vol. **10,** pp. e2022EA002723.

Mateeva, A. *et al.*, 2014a. Distributed acoustic sensing for reservoir monitoring with vertical seismic profiling, *Geophys. Prospect.,* **62**(4), 679–692.

Mateeva, A. *et al.*, 2014b. Distributed acoustic sensing for reservoir monitoring with vertical seismic profiling, *Geophys. Prospect.,* **62,** 679–692 (4-Vertical Seismic Profiling and Microseismicity Frontiers).

Matsumoto, H. *et al.*, 2021. Detection of hydroacoustic signals on a fiber-optic submarine cable, *Sci. Rep.,* **11**(1), 2797.

Mazur, M., Karrenbach, M., Fontaine, N. K., Ryf, R., Kamalov, V., Dallachiesa, L., Jonsson, Ö., Hlynsson, A. A., Chen, H. & Winter, D 2024. *Global seismic monitoring using operational subsea cable,* preprint arXiv:2409.19827(arXiv:2409.19827).

Medwin, H. & Clay, C.S., 1997. *Fundamentals of Acoustical Oceanography,* Academic Press.

Nardone, S., Lindgren, A. & Gong, K., 1984. Fundamental properties and performance of conventional bearings-only target motion analysis, *IEEE Trans. Autom. Control,* **29**(9), 775–787.

Nayak, A., Ajo-Franklin, J. & Team I. V. D.F., 2021. Distributed acoustic sensing using dark fiber for array detection of regional earthquakes, *Seismol. Soc. Am.,* **92**(4), 2441–2452.

Parker, T., Shatalin, S. & Farhadiroushan, M., 2014. Distributed acoustic sensing–a new tool for seismic applications, *First Break,* **32**(2).

Passerieux, J., Pillon, D., Blanc-Benon, P. & Jaufret, C., 1988. Target motion analysis with bearings and frequencies measurements, in *Twenty-Second Asilomar Conference on Signals, Systems and Computers,* Vol. **1,** pp. 458–462, IEEE.

Pelaez Quiñones, J.D. *et al.*, 2023. High resolution seafloor thermometry for internal wave and upwelling monitoring using distributed acoustic sensing, *Sci. Rep.,* **13**(1), 17459.

Pillon, D. & Jauffret, C., 2005. *Trajectographie passive par mesure d'angle,* Ed. Techniques Ingénieur, Saint-Denis, France.

Pratt, R.G., Shin, C. & Hick, G., 1998. Gauss–Newton and full Newton methods in frequency–space seismic waveform inversion, *Geophys. J. Int.,* **133**(2), 341–362.

Rao, Y., Wang, Z., Wu, H., Ran, Z. & Han, B., 2021. Recent advances in phase-sensitive optical time domain reflectometry (ϕ-OTDR), *Photon. Sensors,* **11,** 1–30.

Rivet, D., de Cacqueray, B., Sladen, A., Roques, A. & Calbris, G., 2021. Preliminary assessment of ship detection and trajectory evaluation using distributed acoustic sensing on an optical fiber telecom cable, *J. Acoust. Soc. Am.,* **149**(4), 2615–2627.

Sabra, K.G., Roux, P., Thode, A.M., D'Spain, G.L., Hodgkiss, W. & Kuperman, W., 2005. Using ocean ambient noise for array self-localization and self-synchronization, *IEEE J. Ocean. Eng.,* **30**(2), 338–347.

Shao, J., Wang, Y., Zhang, Y., Zhang, X. & Zhang, C., 2025. Tracking moving ships using distributed acoustic sensing data, *IEEE Geosci. Remote Sens. Lett.,* **22,** 1–5.

Sladen, A., Rivet, D., Ampuero, J.P., De Barros, L., Hello, Y., Calbris, G. & Lamare, P., 2019. Distributed sensing of earthquakes and ocean-solid earth interactions on seafloor telecom cables, *Nat. Commun.,* **10**(1), 1–8.

Taweesintananon, K. *et al.*, 2023. Distributed acoustic sensing of ocean-bottom seismo-acoustics and distant storms: a case study from Svalbard, Norway, *Geophysics,* **88**(3), B135–B150.

Trabattoni, A., Barruol, G., Dreo, R., Boudraa, A. & Fontaine, F.R., 2020. Orienting and locating ocean-bottom seismometers from ship noise analysis, *Geophys. J. Int.,* **220**(3), 1774–1790.

Trabattoni, A., Vernet, C., van den Ende, M., Baillet, M., Potin, B. & Rivet, D., 2024. Sediment corrections for distributed acoustic sensing, *J. geophys. Res.: Solid Earth,* **129**(10), e2024JB029054.

van den Ende, M.P. & Ampuero, J.-P., 2021. Evaluating seismic beamforming capabilities of distributed acoustic sensing arrays, *Solid Earth,* **12**(4), 915–934.

Van Veen, B.D. & Buckley, K.M., 1988. Beam forming: a versatile approach to spatial filtering, *IEEE Assp Magaz.,* **5**(2), 4–24.

Waagaard, O.H., Rønnekleiv, E., Haukanes, A., Stabo-Eeg, F., Thingbø, D., Forbord, S., Aasen, S.E. & Brenne, J.K., 2021. Real-time low noise distributed acoustic sensing in 171 km low loss fiber, *OSA Continuum,* **4**(2), 688–701.

Williams, E.F., Fernández-Ruiz, M.R., Magalhaes, R., Vanthillo, R., Zhan, Z., González-Herráez, M. & Martins, H.F., 2019. Distributed sensing of microseisms and teleseisms with submarine dark fibers, *Nat. Commun.,* **10**(1), 5778.